

# Journal of Materials Chemistry A

Materials for energy and sustainability

Accepted Manuscript

This article can be cited before page numbers have been issued, to do this please use: S. Razavi, V. Rahmanian, R. Cai, M. Rukh, S. A. Khan and F. Li, *J. Mater. Chem. A*, 2025, DOI: 10.1039/D4TA08481K.



This is an Accepted Manuscript, which has been through the Royal Society of Chemistry peer review process and has been accepted for publication.

Accepted Manuscripts are published online shortly after acceptance, before technical editing, formatting and proof reading. Using this free service, authors can make their results available to the community, in citable form, before we publish the edited article. We will replace this Accepted Manuscript with the edited and formatted Advance Article as soon as it is available.

You can find more information about Accepted Manuscripts in the [Information for Authors](#).

Please note that technical editing may introduce minor changes to the text and/or graphics, which may alter content. The journal's standard [Terms & Conditions](#) and the [Ethical guidelines](#) still apply. In no event shall the Royal Society of Chemistry be held responsible for any errors or omissions in this Accepted Manuscript or any consequences arising from the use of any information it contains.

# Perovskite Oxides as A New Family of Tunable CO<sub>2</sub> Sorbents

View Article Online  
DOI: 10.1039/D4TA08481K

Syedamin Razavi†, Vahid Rahmanian†, Runxia Cai†, Mahe Rukh†, Saad A Khan†, Fanxing Li\*†

† Chemical and Biomolecular Engineering Department, College of Engineering, North Carolina State University, 911 Partners Way, Raleigh, NC, USA

\*E-mail: [fli5@ncsu.edu](mailto:fli5@ncsu.edu)

## Abstract

CO<sub>2</sub> adsorption by solid sorbents represents an attractive option for carbon capture due to its potential for low energy consumption, ease of operation, and higher stability. This study introduces perovskite oxides as a new family of highly tunable solid sorbents, with remarkable structural and compositional flexibility to tailor their sorption thermodynamics and kinetics. Using Sr<sub>x</sub>La<sub>1-x</sub>FeO<sub>3</sub> (x=0, 0.2, 0.5, and 0.7) as a model system, we demonstrated that varying the A-site composition of the perovskite oxide leads to substantial change in the CO<sub>2</sub> adsorption and desorption behavior, allowing a tunable CO<sub>2</sub> release within a temperature range of 75 to 500+°C. A strong correlation between the oxide surface area and sorption capacity was also established. Despite the low surface area inherent to perovskite oxides, we managed to enhance their surface area from 3 – 5 m<sup>2</sup>/g (prepared by a salt assisted reactive grinding method) to ~30 m<sup>2</sup>/g using an electrospun nanofibers. Sr<sub>0.2</sub>La<sub>0.8</sub>FeO<sub>3</sub> prepared via electrospinning exhibited a relatively moderate desorption temperature (onset: 120 °C, peak: 240 °C) and a CO<sub>2</sub> sorption capacity of 0.68 wt.%. Analysis of the adsorption isotherms indicates that CO<sub>2</sub> is chemisorbed on the Sr<sub>0.2</sub>La<sub>0.8</sub>FeO<sub>3</sub> sorbent at low CO<sub>2</sub> partial pressures (0-1 kPa). Physisorption becomes dominant at higher pressures. Transmission electron microscopy (TEM) characterizations revealed that perovskite synthesis via the electrospinning method results in the formation of perovskite nanorods. X-ray photoelectron spectroscopy indicates significantly higher surface La concentration when compared to oxides prepared with conventional methods. It was further determined that higher surface La concentration is highly desirable for reversible CO<sub>2</sub> sorption. This study demonstrates the tunability of perovskite oxides as a new family of CO<sub>2</sub> sorbent materials and the potential to further enhance their surface area towards practical applications in CO<sub>2</sub> capture and utilization.

**Keywords:** Sorbents, CO<sub>2</sub> capture, CO<sub>2</sub> adsorption, Perovskite



## 1. Introduction

View Article Online  
DOI: 10.1039/D4TA08481K

A primary driving force behind global climate change is the accumulation of carbon dioxide (CO<sub>2</sub>) in the Earth's atmosphere. As per the Intergovernmental Panel on Climate Change (IPCC), if no significant intervention occurs, CO<sub>2</sub> emissions is anticipated to surge from the current rate of 36 Gt/yr to a range between 48 and 55 Gt/yr by 2050.<sup>1</sup> This rise in emissions is primarily attributed to a substantial increase in energy demand, which is projected to grow by 40% to 150% during the same period. Recovering from an unavoidable excess of atmospheric CO<sub>2</sub> concentrations demands proactive removal of CO<sub>2</sub>.<sup>2</sup> Achieving this necessitates the deployment of technologies capable of effectively capturing and permanently eliminating CO<sub>2</sub> from the atmosphere.<sup>3</sup>

The primary technologies investigated for CO<sub>2</sub> capture include cryogenic distillation, membrane separation, liquid absorption, and solid adsorption.<sup>4</sup> Cryogenic distillation imposes significant limitations on CO<sub>2</sub> capture due to its high energy requirements and the need for an initial step to eliminate compounds such as H<sub>2</sub>O, SO<sub>x</sub>, and NO<sub>x</sub>.<sup>4</sup> Membrane separation is efficient when dealing with high concentrations of CO<sub>2</sub>. However, its effectiveness and selectivity decline when CO<sub>2</sub> is not a substantial component in the stream. Solvent absorption is a well-established technology for CO<sub>2</sub> capture.<sup>4</sup> However, it comes with a significant energy cost for solvent regeneration and is susceptible to corrosion issues and volatility concerns.<sup>5-7</sup> In this context, adsorption by solid sorbents emerges as an appealing alternative which offers potential to reduce the energy expenditure and to mitigate corrosion concerns. Its efficiency, coupled with the simplicity of operation, makes it a promising option for carbon capture from diluted CO<sub>2</sub> streams.<sup>4</sup>

Capturing CO<sub>2</sub> from ambient air, also known as Direct Air Capture (DAC), can complement point-source capture by addressing emissions from dispersed sources that are not reachable through point-source capture methods.<sup>8-10</sup> Additionally, DAC can compensate for any residual emissions that escape during point-source capture.<sup>8-10</sup> The majority of air capture methods employ solid sorbents. Each of the sorbents under investigation utilizes one of two potential adsorption mechanisms: physical or chemical adsorption. Physisorption involves the attraction of target molecules to the surface of pore walls within a sorbent with high surface area, facilitated by van der Waals forces.<sup>11</sup> The heat of adsorption in physisorption is relatively low, only slightly exceeding the heat of sublimation of the adsorbate. In chemisorption, the target gas undergoes a covalent chemical reaction to bind to specific sites on the sorbent, resulting in a significantly higher heat of adsorption that is approximately equivalent to the heat of reaction.<sup>11</sup> Notable adsorbents in physical adsorption include zeolites, activated carbon, alumina, and metal-organic frameworks.<sup>12</sup> Their performance can be notably reduced by high humidity and elevated temperatures, especially in the cases of activated carbon and zeolites.<sup>4, 13</sup> MOFs offer the advantage of being highly flexible when it comes to their shape, pore structure, pore size, and surface properties.<sup>11</sup> Like most sorbents, their sorption capacity and selectivity are influenced by temperature and humidity. In general, MOFs are better suited for storage purposes rather than for the capture or separation of CO<sub>2</sub>.<sup>11, 14</sup> The heat of adsorption of carbon dioxide on these types of sorbents ranges from -25 to -40 kJ/mole, close to the heat of sublimation (~25 kJ/mole).<sup>11, 12</sup> This low heat of adsorption reduces the amount of energy needed to desorb a given quantity of carbon dioxide. Conversely, solid sorbents that capture carbon dioxide via a chemical process, such as bonding with an amine grafted or coated onto



the sorbent's surface, exhibit significantly higher heats of adsorption. Depending on the specific amine employed, the heat of adsorption typically range between -60 and -100 kJ/mol.<sup>11</sup>

View Article Online

DOI: 10.1039/D4TA08481K

This article reports perovskite oxides as a new family of solid sorbents for CO<sub>2</sub> capture. Perovskites are appealing due to their remarkable stability and high compositional and structural flexibility, allowing for tunability in terms of their surface and bulk properties.<sup>15-19</sup> Despite their flexibility and applications in thermal and electro catalysis, ceramic membranes, sensing, etc.<sup>20-22</sup> Perovskite oxides have not been explored as CO<sub>2</sub> sorbents at low temperatures. Meanwhile, a number of previous studies have shown that alkali earth cations in perovskite oxides tend to enrich on the perovskite surface.<sup>23-28</sup> This can lead to strong interaction with CO<sub>2</sub>.<sup>23-28</sup> Although formation of bulk carbonate phases is not desirable, surface interactions between CO<sub>2</sub> and the surface alkali earth cations, whose coordination environment may be tunable by varying the perovskite composition, can offer interesting opportunities. In our current investigation, we utilized Sr<sub>x</sub>La<sub>1-x</sub>FeO<sub>3</sub> (where x=0, 0.2, 0.5, and 0.7) as a model system to illustrate how altering the A-site composition of perovskite oxide can significantly affect the behavior of CO<sub>2</sub> adsorption and desorption. This variation allowed us to achieve adjustable CO<sub>2</sub> release within a temperature range spanning from 180 to over 500°C. We established a strong correlation between the surface area of the oxide and its sorption capacity. By employing an electrospinning method to create nanofibers known for their high surface areas<sup>29, 30</sup>, we successfully increased the surface area from 3 to 5 m<sup>2</sup>/g (achieved through a salt-assisted reactive grinding method) to approximately 30 m<sup>2</sup>/g, resulting in significant increase in the CO<sub>2</sub> capture capacity (up to 0.68 wt.%). This investigation highlights the potential of perovskite oxides as a customizable category of CO<sub>2</sub> sorbent materials, with the possibility of further enhancing their surface area for practical applications in CO<sub>2</sub> capture as well as combined CO<sub>2</sub> capture and utilization.



## 2. Experimental section

### 2.1 Synthesis of $\text{Sr}_x\text{La}_{1-x}\text{FeO}_3$ sorbents

**Solid-state method:** Perovskite oxides were synthesized using a solid-state method. In a typical synthesis of  $\text{Sr}_x\text{La}_{1-x}\text{FeO}_3$ , we weighed stoichiometric amounts of  $\text{SrCO}_3$ ,  $\text{La}_2\text{O}_3$ , and  $\text{Fe}_2\text{O}_3$ , and placed them in a stainless-steel sample jar. Subsequently, we added 3 mm  $\text{ZrO}_2$  beads to the jar in a mass ratio of 5:1. To prevent the powders from adhering to the stainless-steel sample jar, we added 9 mL of ethanol (>99 vol% purity) to the mixture. The mixture was then ball-milled at 1200 RPM for 3 hours. Afterward, we dried the resulting wet mixture in the stainless-steel sample jar at 130 °C for 30 minutes to remove the ethanol. Following this step, the powder mixture was separated from the  $\text{ZrO}_2$  beads and calcined at 1000 °C in a muffle furnace for 10 hours to obtain the perovskite structure. Both the heating and cooling rates were set at 3 °C/min. Finally, the perovskite samples were sieved to particle sizes below 250  $\mu\text{m}$  for TGA testing. To enhance the surface area of perovskite materials, we employed the salt-grinding method, aiming to create a porous structure. The perovskite was blended with  $\text{K}_2\text{CO}_3$  and 3mm  $\text{ZrO}_2$  beads inside a stainless-steel sample jar, maintaining a specific mass ratio. Subsequently, the jar underwent ball milling at 1200 RPM for 24 hours, utilizing a high-energy ball mill to augment porosity. The resultant powder mixtures were subjected to a water rinse to eliminate  $\text{K}_2\text{CO}_3$ . Subsequently, the remaining moist particles were dried in an oven at 130°C to yield the high-porosity perovskite materials.

**Electrospinning method:** The synthesis of  $\text{Sr}_{0.2}\text{La}_{0.8}\text{FeO}_3$  perovskite oxide was carried out through the electrospinning method using metal precursors and a polymer solution. Details of this technique are established elsewhere<sup>29, 30</sup>. Briefly, a polymer solution is pumped through a syringe in this method. The ejected solution is subjected to an electric field causing it elongate into nanofibers. These nanofibers are collected as a nonwoven fibrous web on a collector placed at specified distance from the syringe tip.<sup>31</sup> In our case, a solution was prepared by fully dissolving  $\text{La}(\text{NO}_3)_3 \cdot 6\text{H}_2\text{O}$ ,  $\text{Sr}(\text{NO}_3)_2$ , and  $\text{Fe}(\text{NO}_3)_3 \cdot 9\text{H}_2\text{O}$  in a mixture of  $\text{H}_2\text{O}$ ,  $\text{C}_2\text{H}_5\text{OH}$  (Ethanol), and DMF (Dimethylformamide) in a 2:5:5 mass ratio. Additionally, 15.5 wt% PVP (polyvinylpyrrolidone) was added to the solution. The electrospinning process was conducted with a distance of 15 cm between the needle tip of the syringe and a grounded aluminum foil collector. An applied voltage of 20 kV was used, which was generated by a custom-made D.C. power supply. To control the injection rate, a syringe pump (New Era Pump System Inc., Model no. NE-300) was employed, maintaining a rate of 0.5 mL min<sup>-1</sup>. Following the electrospinning step, the resulting fibers were dried at 80°C in an oven overnight and then collected. To obtain the  $\text{Sr}_{0.2}\text{La}_{0.8}\text{FeO}_3$  perovskite oxide, the collected fibers were subjected to calcination at 650°C for 3 hours, employing a heating rate of 3°C min<sup>-1</sup> in an air. It should be noted while our approach here entailed a lab scale setup, Industrial production lines for electrospinning have been designed and implemented industrially, enabling the large-scale manufacturing of electrospun nanofibers for applications such as air and water filtration, biomedical devices, and energy storage systems. Many of these approaches use multi-needle or nozzle-less systems, incorporating real-time monitoring for quality assurance, and developing solvent-free or environmentally friendly methods to reduce costs and minimize environmental impact.<sup>32, 33</sup>

### Sorbent evaluation





The CO<sub>2</sub> adsorption capacity of Sr<sub>x</sub>La<sub>1-x</sub>FeO<sub>3</sub> was investigated using a TA Instruments SDT 650 thermogravimetric analyzer (TGA) at a temperature of 35°C. Samples weighing between 30-40 mg were loaded into an Al<sub>2</sub>O<sub>3</sub> crucible with a 6.5 mm inner diameter and subsequently placed inside the TGA apparatus. The samples were then subjected to heating at a rate of 20°C per minute until reaching 550°C under an Ar atmosphere with a purity of 99.999%, and a flow rate of 200 mL/min. This heating step was maintained for 60 minutes to eliminate any adsorbed species. Following the cooling of the samples to the desired analysis temperature, a 60-minute equilibration period was allowed before switching the gas flow to a mixture comprising 10% CO<sub>2</sub> and 90% Ar at a flow rate of 200 mL/min. This CO<sub>2</sub> exposure was conducted for a duration of 30 minutes. Subsequently, to initiate the desorption step and release CO<sub>2</sub> species from the surface, the temperature was increased, and pure argon was employed. The cyclic adsorption and desorption stability experiments were conducted under similar conditions.

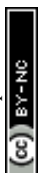
### 2.3 Sorbent Characterizations

**X-Ray diffraction analysis (XRD):** The crystal structures of the samples were determined using an Empyrean PANalytical X-ray diffraction (XRD) instrument, which utilized Cu-K $\alpha$  radiation with a wavelength ( $\lambda$ ) of 1.5406 Å. The XRD apparatus was operated at 45 kilovolts (kV) and 40 milliamperes (mA). The scanning process covered a range of  $2\theta$  values from 10° to 90°, employing a step size of 0.0262° for each measurement and a holding time of 0.2 seconds per step. To identify the XRD phases present in the samples, Highscore Plus software was employed.

**Surface area measurement:** The Brunauer-Emmett Teller (BET) surface areas (denoted as SBET) and pore volumes of the samples were assessed using nitrogen sorption analysis, which was carried out with a Micromeritics ASAP 2020 instrument at a temperature of 77 K. Before commencing the measurements, the samples underwent a degassing process, reducing the pressure to less than 5 mm Hg, and were heated at 200°C for a duration of 10 hours to remove any residual gases and impurities. The determination of SBET followed the multipoint BET method within the pressure range of 0 to 120 kPa, allowing for a comprehensive characterization of the samples' surface properties and porosity.

**CO<sub>2</sub> adsorption isotherms:** The study involved examining the adsorption of CO<sub>2</sub> at a low temperature of 0°C and 25°C, employing a precise Micromeritics ASAP 2020 instrument. To ensure the accuracy of the measurements, a meticulous sample preparation procedure was followed. Initially, the samples were subjected to a rigorous degassing process, which effectively reduced the pressure within the system to less than 5 mm Hg. Subsequently, these samples were carefully heated to a temperature of 200°C for a duration of 10 hours. This thermal treatment was essential to eliminate any residual gases and impurities, thereby ensuring the purity of the samples. Once the samples were suitably prepared, the determination of CO<sub>2</sub> adsorption was carried out across a wide range of pressure conditions, spanning from 0 to 120 kPa.

**Electron microscopy:** High-resolution transmission electron microscopy (HRTEM) and scanning TEM high-angle annular dark-field (STEM-HAADF) equipped with energy dispersive X-ray (EDX) tomography to survey elemental mappings were employed to unveil morphology and elemental composition (FischerScientific Talos, 200 kV). Additionally, it was equipped with a specialized liquid nitrogen-cooled energy-dispersive X-ray spectroscopy (EDS) detector to facilitate elemental analysis. To prepare the samples for analysis, they were



initially transformed into fine powders. Subsequently, these powders were dispersed in ethanol using ultrasonication, ensuring an even distribution. The resulting suspension was then carefully deposited onto a Cu grid coated with holey carbon. Finally, the prepared samples were left to air dry under standard ambient conditions before HRTEM analysis was performed.

The surface morphology of the catalyst was analyzed using a Thermo Fisher Scientific Verios 460L Field Emission Scanning Electron Microscopy (SEM) operating at 2 kV. Samples were mounted onto conductive carbon tape, and secondary electron images were captured without the application of any coating.

**X-ray photoelectron spectroscopy (XPS):** XPS spectra were obtained using the following parameters: a current of 10 mA and an accelerating voltage of 15 kV. The data acquisition involved a pass energy of 20 eV and a step size of 0.1 eV. Subsequently, peak deconvolution was carried out utilizing Casa XPS software, developed by Casa Software Ltd. in the United Kingdom. This process included the application of a Shirley background subtraction method and the use of mixed Gaussian–Lorentzian functions to enhance peak resolution. Furthermore, the binding energies in the obtained spectra were calibrated with reference to the C 1s peak, which was assigned a value of 285 eV.

**Fourier-transform infrared spectroscopy (FTIR):** To obtain *ex situ* IR data, we employed FTIR spectroscopy using a Thermo Fisher Nicolet iS50 ATR instrument. The process began by introducing the freshly prepared sample into the *ex situ* cell. To establish the background spectrum, the instrument recorded the spectrum from the fresh sample, which was subsequently automatically subtracted from the sample spectrum. For the sample spectrum, we subjected the sample to a pre-treatment phase within a TGA (Thermogravimetric Analyzer). During this phase, we introduced pure Ar (99.99%) as the carrier gas. Following this, we conducted the first cycle of CO<sub>2</sub> adsorption using a gas mixture of CO<sub>2</sub>/Ar (10% CO<sub>2</sub>, 90% Ar) at a flow rate of 200 mL/min. This adsorption process was carried out for a duration of 30 minutes at a temperature of 35 °C. Subsequently, we stopped the TGA and transferred the treated sample to the *ex situ* IR setup to collect the sample spectrum.

In order to collect *in situ* IR data, FTIR spectroscopy was employed using a Thermo Fisher Nicolet iS50 FTIR, which was equipped with a DiffusIR sample chamber from Pike Technologies. The process began by loading the sample into the *in situ* cell and purging it with Ar gas at 600 °C for a duration of 30 minutes. After this step, the sample was cooled to a temperature of 25 °C. To obtain the background spectrum, the instrument collected the spectrum in an Ar stream at 25 °C, which was then automatically subtracted from the sample spectrum. CO<sub>2</sub> reaction gas was introduced into the reaction cell at a flow rate of 40 mL/min, and spectra were collected repeatedly until the spectrum curve stabilized.



### 3. Results and Discussion

#### 3.1 Sorbent phase purity and effect of preparation methods on sorbents surface areas

To determine the effect of A-site compositions on perovskites' CO<sub>2</sub> sorption properties, a simple solid state synthesis method was adopted first to prepare the perovskite samples for screening purpose. This is followed with X-Ray diffraction analysis (XRD) to confirm their phase purity. As shown in **Figure 1a**, the XRD patterns for all the synthesized samples exhibited well-defined diffraction peaks, signifying their phase purity.

One of the key challenges associated with the use of perovskites as adsorbents for CO<sub>2</sub> capture is their inherently low surface area, which consequently results in a limited adsorption capacity. To address this limitation, we adopted two strategies, i.e. reactive grinding and creating nanofibrous structure via electrospinning, to increase their surface area. Using potassium as an alkali additive in reactive grinding increases surface area and adsorption capacity. Electrospinning with surfactants and templates, followed by calcination, creates perovskite oxides with higher surface areas and potentially controllable nanostructures.

**Table 1** summarizes the BET surface areas of Sr<sub>x</sub>La<sub>1-x</sub>FeO<sub>3</sub> (x=0, 0.2, 0.5, 0.7) perovskite oxides before and after grinding with salt. As can be seen, before grinding, the perovskite's surface area averaged 3 to 5 m<sup>2</sup>/g. In comparison, the surface area increased nearly five-fold on average after reactive grinding. To further enhance the surface area of the perovskite, we employed the electrospinning technique. The BET results demonstrated the efficacy of this approach, with the surface area of the as-prepared Sr<sub>0.2</sub>La<sub>0.8</sub>FeO<sub>3</sub> increasing to nearly 30 m<sup>2</sup>/g. This finding underscores the efficacy of electrospinning as a synthesis approach for enhancing the surface area. As illustrated in **Figure 1b** and **Figure 1c**, following the reactive grinding and electrospinning process, the perovskite materials have maintained their phase purity.

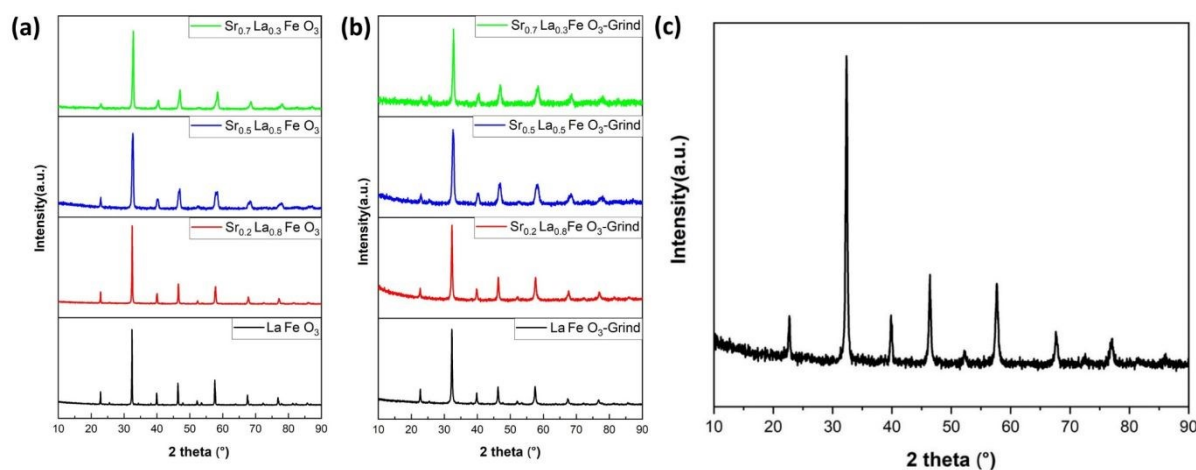


**Figure 1.** XRD results of Sr<sub>x</sub>La<sub>1-x</sub>FeO<sub>3</sub> (x=0, 0.2, 0.5, 0.7) perovskite oxide. (a) Before grinding with salt (b) after grinding with salt. (c) XRD result of Sr<sub>0.2</sub>La<sub>0.8</sub>FeO<sub>3</sub> (Electrospun)

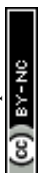




**Table 1**- The results of the BET analysis for perovskite were compared before and after the processes of grinding and electrospinning

Sample	$S_{\text{BET}}$ ( $\text{m}^2/\text{g}$ )	$V_p$ ( $\text{cm}^3/\text{g}$ )	$S_p$ ( $\text{\AA}$ )
La Fe	3.43	0.0091	128.3
$\text{Sr}_{0.2}\text{La}_{0.8}\text{FeO}_3$	2.38	0.0076	143
$\text{Sr}_{0.5}\text{La}_{0.5}\text{FeO}_3$	3.55	0.0079	101.3
$\text{Sr}_{0.7}\text{La}_{0.3}\text{FeO}_3$	2.93	0.0063	108.8
La Fe-Grind	15.76	0.075	164.5
$\text{Sr}_{0.2}\text{La}_{0.8}\text{FeO}_3$ -Grind	15.56	0.098	213
$\text{Sr}_{0.5}\text{La}_{0.5}\text{FeO}_3$ -Grind	23.36	0.132	206
$\text{Sr}_{0.7}\text{La}_{0.3}\text{FeO}_3$ -Grind	14.18	0.079	201
$\text{Sr}_{0.2}\text{La}_{0.8}\text{FeO}_3$ - Electrospun	29.55	0.119	143.5

### 3.2 Tunability of sorbents' surface properties for $\text{CO}_2$ adsorption

The Sr percentage in the perovskite A-site is fully adjustable in  $\text{Sr}_x\text{La}_{1-x}\text{FeO}_3$  perovskite oxides. Given the high basicity of  $\text{Sr}^{2+}$ , adjusting this ratio significantly influences the surface characteristics and sorption properties of the sorbents. Our research demonstrates that increasing the amount of strontium in the A-site makes the perovskite surface progressively more basic, facilitating the formation of more strontium carbonate and raising the desorption temperature, as shown in **Figure 2a**. TGA results indicate that the onset temperature for  $\text{CO}_2$  desorption, determined based on the second order derivative of the weight as a function of temperature, increased with increasing strontium content from 75 to 140 °C. Meanwhile, the peak desorption temperature also varied significantly with the strontium content: the  $\text{Sr}_{0.2}\text{La}_{0.8}\text{FeO}_3$  sample desorbs at around 120°C (180°C after grinding, likely due to residual potassium), while the  $\text{Sr}_{0.7}\text{La}_{0.3}\text{FeO}_3$  sample desorbs at over 500°C (**Figure 2b**). Thus, increasing strontium in the A-site primarily elevates the desorption temperature, with only a modest impact on adsorption capacity. Since a lower desorption temperature leads to lower energy consumption, we selected the sample with the lowest strontium content and then focused on enhancing the perovskite's surface area to improve carbon dioxide adsorption.

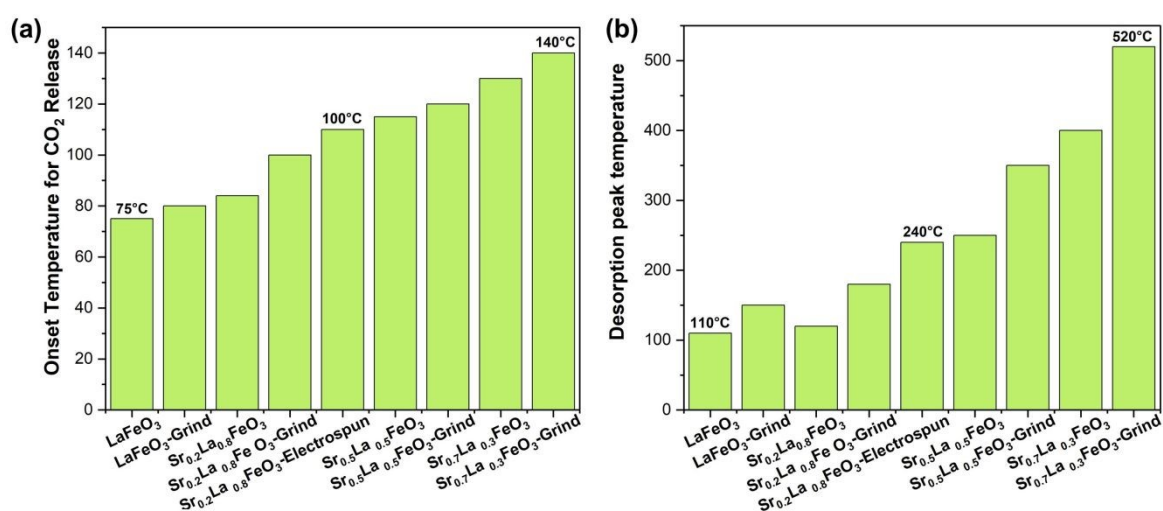


**Figure 2.** TGA results of  $\text{Sr}_x\text{La}_{1-x}\text{FeO}_3$  perovskite oxide. (a) Onset temperature for  $\text{CO}_2$  release of  $\text{Sr}_x\text{La}_{1-x}\text{FeO}_3$  perovskite oxide ( $x=0, 0.2, 0.5, 0.7$ ). (b) Desorption peak temperature of  $\text{Sr}_x\text{La}_{1-x}\text{FeO}_3$  perovskite oxide ( $x=0, 0.2, 0.5, 0.7$ ).

View Article Online  
DOI: 10.1039/D4TA08481K

### 3.3 Effect of synthesis method on sorption capacity

Although sorbents prepared via SSR showed excellent phase purity and tunable sorption properties, their sorption capacities are rather limited ( $\sim 0.05$  wt.%). This is largely due to their low surface areas which are intrinsic to perovskite oxides. As shown in Table 1. We chose the  $\text{Sr}_{0.2}\text{La}_{0.8}\text{FeO}_3$  sample and increased its surface area by grinding it with potassium carbonate. Before grinding, the perovskite demonstrates an adsorption capacity of  $\sim 0.05$  wt.%, as revealed by TGA analysis. Subsequent to the grinding process, the adsorption capacity more than tripled to  $\sim 0.18$  wt.%. **Figure 3a** shows the cyclic stability of the sorbent. As can be seen, the adsorption capacity remained constant throughout the test, confirming its durability.

To further enhance the surface area of the perovskite, we employed the electrospinning technique. In this method, our objective is to determine the optimal calcination temperature that maximizes both phase purity and surface area. We conducted *in situ* XRD across a temperature range spanning from 400 to 700 °C. At 700 °C, we observed a surface area of approximately 17  $\text{m}^2/\text{g}$ , accompanied by the presence of a pure phase. However, at 550 °C, while we achieved a surface area of around 35  $\text{m}^2/\text{g}$ , we did not attain phase purity. It was therefore determined that the most suitable calcination temperature is 650 °C, as it allows us to achieve both phase purity and a high surface area (**Figure 3b**). We conducted a cyclic experiment using TGA on  $\text{Sr}_{0.2}\text{La}_{0.8}\text{FeO}_3$  synthesized through the electrospinning method. This material exhibited excellent stability throughout the repeated cycles of adsorption and desorption (**Figure 3c** and **Figure S1a**) under a low concentration of carbon dioxide (0.4 vol.%  $\text{CO}_2$  balance Ar). As shown in **Figure 3c**, the sample demonstrates notable stability, with its adsorption capacity exhibiting consistency across 55 cycles. This observation underscores the effectiveness of the  $\text{Sr}_{0.2}\text{La}_{0.8}\text{FeO}_3$  sorbent (synthesized via electrospinning).

As can be seen from **Figure 3d**, sorption capacity is directly related to the sorbent surface area. In fact, sorbent capacities are proportional to their surface areas for the  $\text{Sr}_{0.2}\text{La}_{0.8}\text{FeO}_3$  samples prepared by SSR and reactive grinding. However, the electrospun sample does not follow this linear correlation: its sorption capacity ( $\sim 0.68$  wt.%) is more than three times greater than that achieved through the reactive grinding method, although its surface area only doubled. This variance in adsorption capacity is therefore likely attributable to differences in both surface area and nature of the surface adsorption sites. The difference in surface properties is further discussed in the next section.



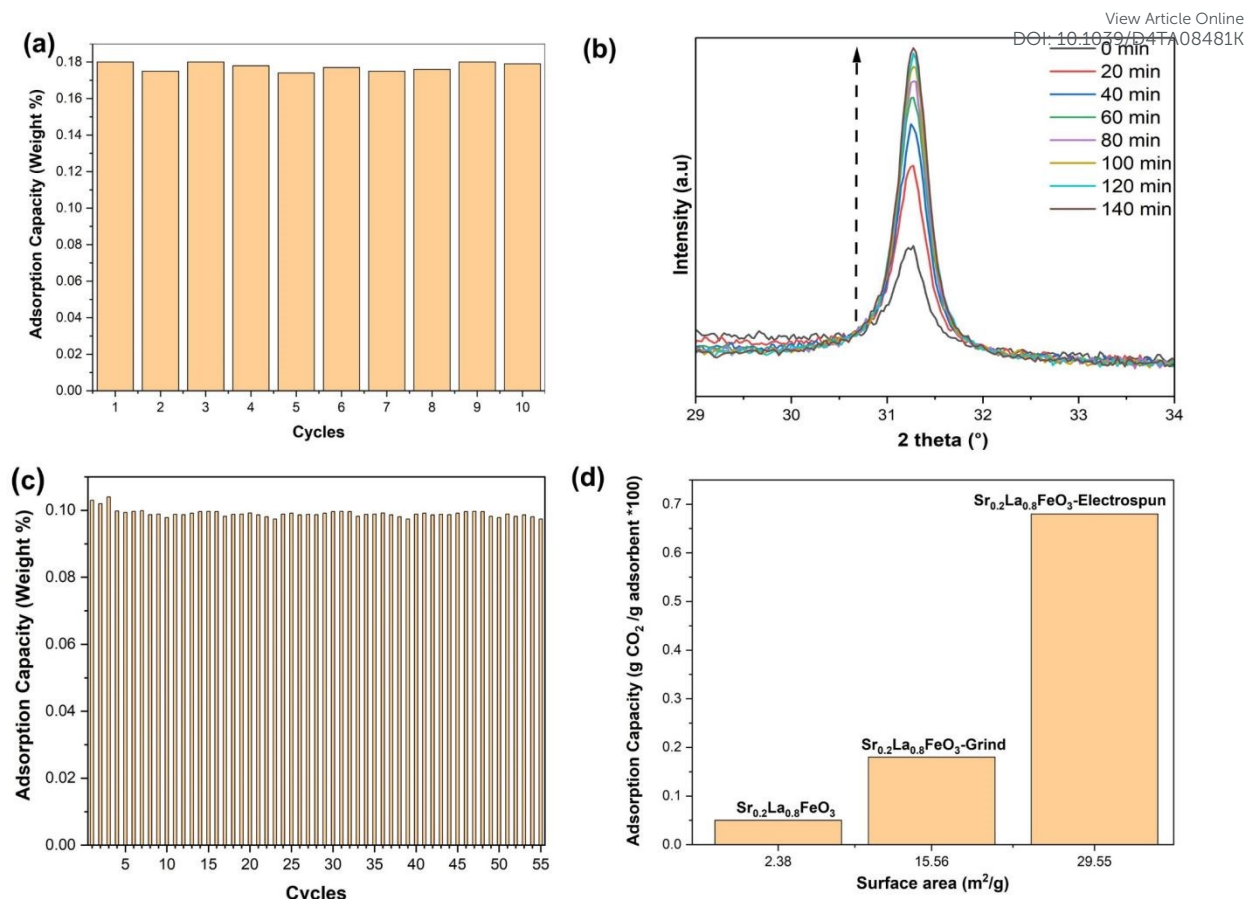
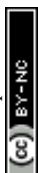


**Figure 3.** (a) Cyclic CO<sub>2</sub> uptake of Sr<sub>0.2</sub>La<sub>0.8</sub>FeO<sub>3</sub> (Reactive grinding) at 35 °C using CO<sub>2</sub>/Ar (10/90) via a gravimetric method. (b) *In-situ* XRD analysis on Sr<sub>0.2</sub>La<sub>0.8</sub>FeO<sub>3</sub> (Electrospun) at 650°C over varying exposure times. (c) Cyclic CO<sub>2</sub> uptake of Sr<sub>0.2</sub>La<sub>0.8</sub>FeO<sub>3</sub> (Electrospun) at 35 °C using 0.4 % CO<sub>2</sub> via a gravimetric method. (d) Correlation between surface area and adsorption capacity for Sr<sub>0.2</sub>La<sub>0.8</sub>FeO<sub>3</sub> (Grinding with salt) and Sr<sub>0.2</sub>La<sub>0.8</sub>FeO<sub>3</sub> (Electrospun).

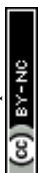


## 2.4 Effect of synthesis method on sorbents' surface and sorption properties

The SEM image in **Figure 4a** depicts the electrospun nanofibrous mat before the calcination process of  $\text{Sr}_{0.2}\text{La}_{0.8}\text{FeO}_3$ , confirming that the electrospinning conditions indeed produce fibers that are devoid of aggregates, demonstrating a homogeneous structure.<sup>34</sup> However, post-calcination, the fibrous mat is broken up, revealing a rod-like or short nanofiber shape, as evidenced in **Figure 4b**. This is akin to shearing nanofiber dispersions to break them into smaller fibers that still provide a high surface area.<sup>35, 36</sup> This transformation occurs during the calcination process, wherein the decomposition of polyvinylpyrrolidone (PVP) takes place, and the metal precursors stabilize to form a distinctive nanorod structure (**Figure 4c**).<sup>37</sup> To further characterize the material, an elemental analysis was performed using energy-dispersive X-ray spectroscopy (EDS), resulting in the distribution of atoms represented in the color map depicted in **Figure 4d**. The EDS element images confirm the presence of all elements within the  $\text{Sr}_{0.2}\text{La}_{0.8}\text{FeO}_3$  composition, illustrating their well-dispersed distribution throughout the nanorod structure.<sup>37</sup> The high aspect ratios of the nanorod structure result in a greater surface area compared to cluster materials obtained through reactive grinding, as shown in the TEM images of ground materials in **Figure S2**. In addition to offering more active sites for  $\text{CO}_2$  adsorption, the change in morphology and hence surface termination/elemental compositions can potentially alter the surface adsorption chemistry, as elaborated next.

XPS analysis was conducted to assess the near surface elemental distribution of the samples prepared via electrospinning and reactive grinding methods. According to elemental composition analysis via XPS (**Figure 4e**), the atomic percentages (carbon and oxygen free basis) are as follows: for  $\text{Sr}_{0.2}\text{La}_{0.8}\text{FeO}_3$  (synthesized via reactive grinding): the composition is 7.84% for Sr, 31.03% for La, and 61.24% for Fe. For  $\text{Sr}_{0.2}\text{La}_{0.8}\text{FeO}_3$  (synthesized via electrospinning), the composition is 6.65% for Sr, 55.09% for La, and 38.25% for Fe. These results suggest distinct elemental distributions between the two synthesis methods. Notably, electrospinning results in higher surface concentrations of A site cations, i.e. Sr and La, whereas the grinding method shows a higher percentage of Fe. Another interesting aspect is that the electrospun sample exhibited significantly higher near surface La/Sr ratio ( $\sim 8.3$ ) than that of the reactive grinding sample ( $\sim 4$ ). In fact, the near surface Sr concentration is higher in the reactive grinding sample (7.84%) than that in the electrospun sample (6.65%). This points to: (a) the  $\text{CO}_2$  sorption capacity may directly correlate with the surface concentration of A-site cations; (b) La is likely to be responsible for a notable fraction of the observed  $\text{CO}_2$  sorption. The latter is somewhat surprising given that Sr was originally envisioned as the active sites for  $\text{CO}_2$  sorption.

The O 1s spectra for both electrospinning and grinding exhibit two distinct peaks (**Figure 4f**). The peak at the lower binding energy can be attributed to lattice oxygen species ( $\text{O}^{2-}$ )<sup>38, 39, 40, 41</sup>, whereas the high binding energy peak is attributable to oxygen associated with carbonates<sup>42</sup> or hydroxyls<sup>43</sup>. As can be seen, the electrospun sample shows a weaker carbonate peak (high B.E. to low B.E. peak area ratio = 2/3) compared to the ground sample (peak area ratio = 1/1). Further analysis of the Sr 3d region confirms the presence of strontium carbonate ( $\text{SrCO}_3$ ) on both samples (**Figures S3-4**). Regarding the Sr 3d<sub>5/2</sub> region, the broad peak suggests the presence of Sr(II) in various chemical environments. Typically, the dominant peak at 134.46 eV for the electrospinning method and 134.23 eV for the reactive grinding method is attributed





to  $\text{SrCO}_3$ . Additionally, the peak at around 132.37 eV for the reactive grinding method and 132.71 eV for the electrospinning method confirms the presence of strontium oxide (SrO) within the perovskite lattice.<sup>44</sup> On the other hand, in the La 3d region, the binding energies observed at 834.19 eV (La 3d<sub>5/2</sub>) and 838.1 eV (La 3d<sub>3/2</sub>) for the reactive grinding method, and 833.92 eV (La 3d<sub>5/2</sub>) and 837.78 eV (La 3d<sub>3/2</sub>) for electrospinning method, align with the known values for La (III) in similar perovskite structures. These peaks likely correspond to La(III) oxide or hydroxide.<sup>44</sup> These results indicate that the high basicity of the Sr cation may lead to the formation of stable carbonates that are difficult to regeneration/decompose. In comparison, La cations would be largely available for reversible  $\text{CO}_2$  sorption/desorption.

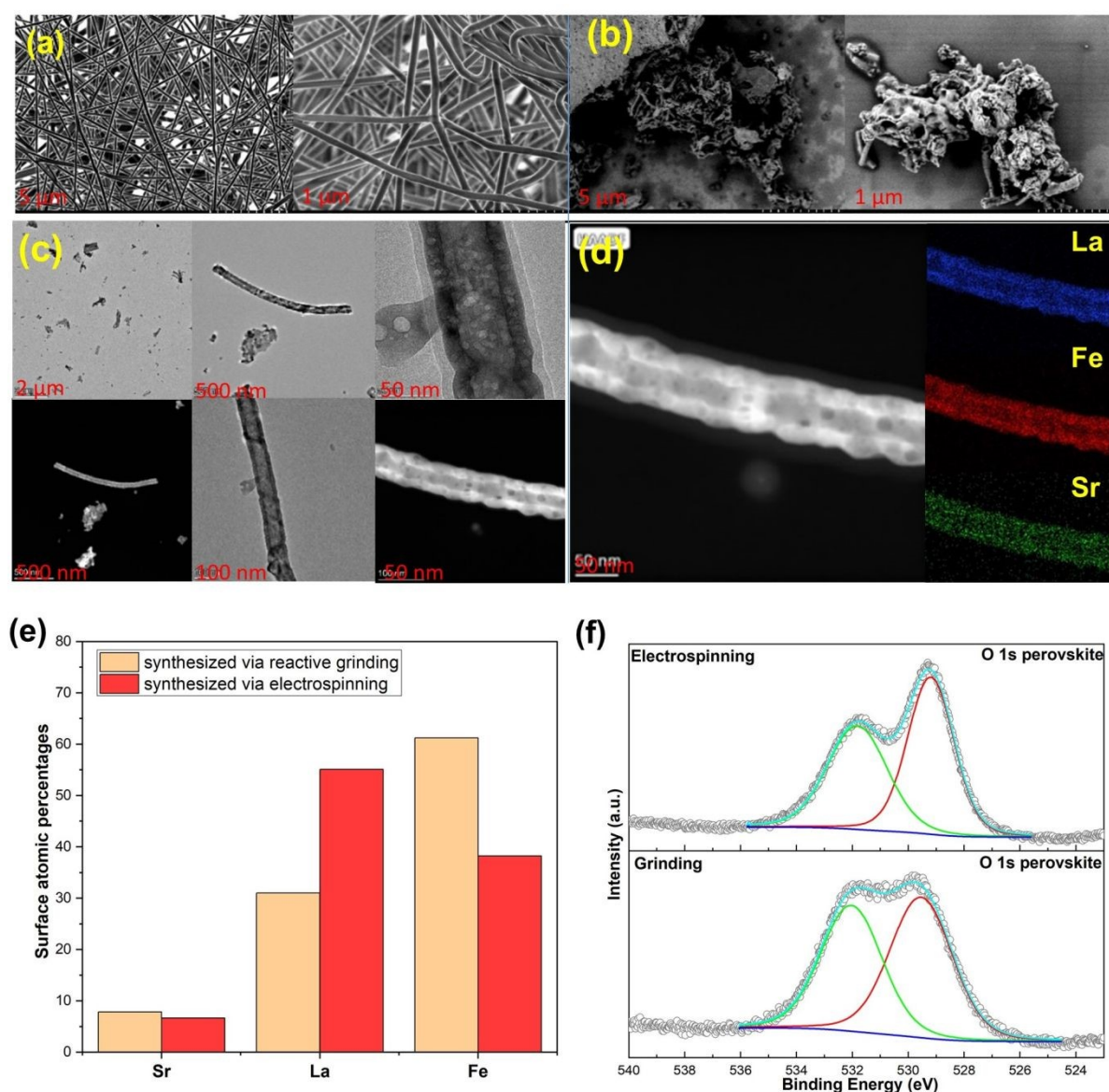


**Figure 4.** (a) SEM image of  $\text{Sr}_{0.2}\text{La}_{0.8}\text{FeO}_3$  prepared by electrospinning before calcination; (b) post-calcination; (c) TEM images of the electrospun sample; (d) corresponding elemental mapping by EDS; (e) Comparison of the XPS derived near surface atomic surface percentages between samples prepared via electrospinning and grinding methods; (f) Comparisons of the O1s spectra of the electrospinning and reactive grinding samples.



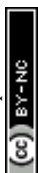


To further clarify the role of surface A-site cations, the adsorption enthalpies of the two sorbents were also measured. This involved calculating the isosteric heat of CO<sub>2</sub> adsorption through the utilization of the Clausius-Clapeyron equivalent adsorption heat equation.<sup>45</sup>

$$q_{st} = RT_1T_2 \frac{\ln\left(\frac{p_1}{p_2}\right)}{T_2 - T_1} \quad (1)$$

The isosteric heat of adsorption ( $q_{st}$ ) is calculated using the formula, where R represents the universal gas constant (8.314 J/mol/K), T ( $T_1 = 298$  K;  $T_2 = 273$  K) denotes the adsorption temperature, and P is the adsorption pressure. The  $q_{st}$  values for the prepared adsorbents are determined based on the CO<sub>2</sub> adsorption data obtained at 0 and 25 °C, CO<sub>2</sub> adsorption was carried out from 0 to 120 kPa, as shown in **Figure 5 (a-b)**. We note that in the case of adsorption isotherm measurement, the surface area normalized adsorption capacities for the electrospun and ground samples are similar. In contrast, the TGA data indicated that the electrospun sample exhibited significantly higher surface normalized CO<sub>2</sub> sorption capacity (nearly 100% higher than that of the ground sample). This is due to differences in experimental conditions: the TGA measurement was performed to determine the reversible sorption capacity under temperature swings and at a relatively low CO<sub>2</sub> partial pressure (0.1 atm). In contrast, the adsorption isotherm was performed at low temperatures for up to 1.2 atm of CO<sub>2</sub>. Since the samples were pretreated at a high temperature to decompose the stable carbonates prior to the isothermal measurement, it is quite possible that some of the stable carbonates that formed during the isothermal measurement would not contribute to the reversible sorption capacity. Additional TGA tests further confirmed this hypothesis as the reactive grinding sample showed a significantly higher amount of stable carbonates that act as a spectator phase and do not contribute to the usable CO<sub>2</sub> capacity under the standard adsorption/desorption conditions (**Figure S6**).

For electrospun Sr<sub>0.2</sub>La<sub>0.8</sub>FeO<sub>3</sub> at adsorption capacities below 0.0375 mmol/g, it is difficult to accurately determine the heat of adsorption due to instrumentation limitations in measuring CO<sub>2</sub> uptake at low pressures (**Figure S7 a/b**). We note that this low-pressure limitation is not an issue for the grinding sample since it requires significantly higher CO<sub>2</sub> partial pressure to achieve the sample adsorption capacity. That said, based on two sets of measurements for the electrospun sample at the low-pressure range (**Figure S7c**), the heat of adsorption for the electrospun sample was approximately 85 kJ/mol at the lowest measurable pressure (corresponding to ~0.028 mmol/g CO<sub>2</sub> uptake). Between 0.028 and 0.035 mmol/g, the heat capacity steadily dropped along with increase in CO<sub>2</sub> uptake, and the average heat of adsorption within this range is ~70 kJ/mol, corresponding to chemisorption. This indicates a strong adsorption affinity, with both data sets clearly supporting a chemisorption process characterized by adsorption enthalpies exceeding 60 kJ/mol. Conversely, for adsorption capacities beyond this threshold, the adsorption enthalpies quickly decrease to below 40 kJ/mol, indicating physisorption. Overall, the  $q_{st}$  value shows a noticeable decline as adsorption progresses, eventually stabilizing nearly 10 kJ/mol for the electrospun Sr<sub>0.2</sub>La<sub>0.8</sub>FeO<sub>3</sub>. This phenomenon occurs likely because CO<sub>2</sub> would preferentially adsorb on stronger adsorption sites, e.g. undercoordinated Sr-O sites. For Sr<sub>0.2</sub>La<sub>0.8</sub>FeO<sub>3</sub> synthesized via reactive grinding, the majority of its adsorption capacity corresponds to chemisorption, with physisorption accounting for only a small fraction of its overall adsorption. The significantly different enthalpy of adsorption profiles between the two samples can potentially be explained by the difference in near surface cation compositions. The XPS results indicate that the electrospun



sample has a higher concentration of La near the surface, which acts as adsorption sites and exhibit lower adsorption energy than Sr. On the other hand, in the ground sample, the high Sr concentration leads to strong adsorption energy. However, a notable fraction of the undercoordinated Sr-O sites would contribute to the formation of stable carbonates that do not contribute to usable CO<sub>2</sub> sorption in a practical thermal swing adsorption process, as indicated from the TGA measurements.

To better understand the difference in the adsorption process between the two samples, we calculated the potential site densities on the 111 and 001 surfaces of the electrospun and grinding sample and compared these with the experimentally measured adsorption capacity. In our calculations, we assumed that the entire surface could adsorb CO<sub>2</sub> molecules, consistent with monolayer adsorption, using a cubic structure with an approximate distance of 6.7 Å between A-site cations. The calculated adsorption capacities per surface area, based on these assumptions, are approximately 0.0041 mmol CO<sub>2</sub>/m<sup>2</sup> for the 001 surface and 0.00429 mmol CO<sub>2</sub>/m<sup>2</sup> for the 111 surface. The experimental adsorption capacities per surface area of Sr<sub>0.2</sub>La<sub>0.8</sub>FeO<sub>3</sub> synthesized via electrospinning and grinding are around 0.0053 mmol CO<sub>2</sub>/m<sup>2</sup> and 0.0051 mmol CO<sub>2</sub>/m<sup>2</sup>, respectively. Based on **Figure 5d**, comparing the experimental and calculated adsorption capacities per surface area indicates that both samples exhibit monolayer adsorption.

To unveil the disparity in the interaction between CO<sub>2</sub> molecules and adsorption sites, FTIR was conducted for both samples. **Figure 5e** shows the *in situ* FTIR spectra of Sr<sub>0.2</sub>La<sub>0.8</sub>FeO<sub>3</sub> (electrospinning) under increasing temperature, measured immediately after 10% CO<sub>2</sub> pulses. At each temperature level, the FTIR results in **Figure 5e** confirm the presence of both monodentate and bidentate carbonate species. As the temperature increases, the absorbance intensity decreases, indicating a decrease in carbonate content. Notably, beyond 175°C, one of the monodentate carbonate peaks diminishes, reflecting its weaker bonding compared to bidentate carbonate. This suggests that bidentate adsorption dominates at low CO<sub>2</sub> coverage. With increasing CO<sub>2</sub> coverage, some bidentate species are transformed into monodentate configuration. The disappearance of the carbonate peaks at 240°C is consistent with the TGA measurements, which showed an onset temperature for CO<sub>2</sub> desorption at 100°C and a peak desorption temperature of 240°C. This further confirms that the high near surface La concentration in the electrospun sample inhibits the formation of stable carbonate species and enhances the reversibility of the CO<sub>2</sub> sorption/desorption. These findings also correspond well with the XPS results and enthalpy of adsorption measurements for the electrospun sample.

To compare the binding of CO<sub>2</sub> on the surface of the electrospinning and grinding samples, we performed the *in-situ* analysis with 10% CO<sub>2</sub> balance Ar flowing at a rate of 40 mL/min operated at 25 °C (**Figure 5f**). The carbonate peaks in these two samples exhibit distinct peak locations, stemming from differing surface properties and structures resulting from the electrospinning and grinding methods employed. The greater distance between the bidentate peaks in the electrospinning sample compared to the grinding sample indicates weaker carbonate species in the electrospinning sample.<sup>46</sup> This corroborates well with the isotherm analysis (**Figure 5 c/d**). Overall, it is evident that the higher surface La concentration in the electrospun sample provides favorable adsorption sites for reversible sorption and desorption of CO<sub>2</sub>. On the other hand, a high surface Sr concentration, e.g. on the reactive grinding sample, would lead to highly stable carbonate species that are not desirable for low temperature CO<sub>2</sub> sorption applications. These findings provide valuable insights into tailoring materials for improved adsorption performance.



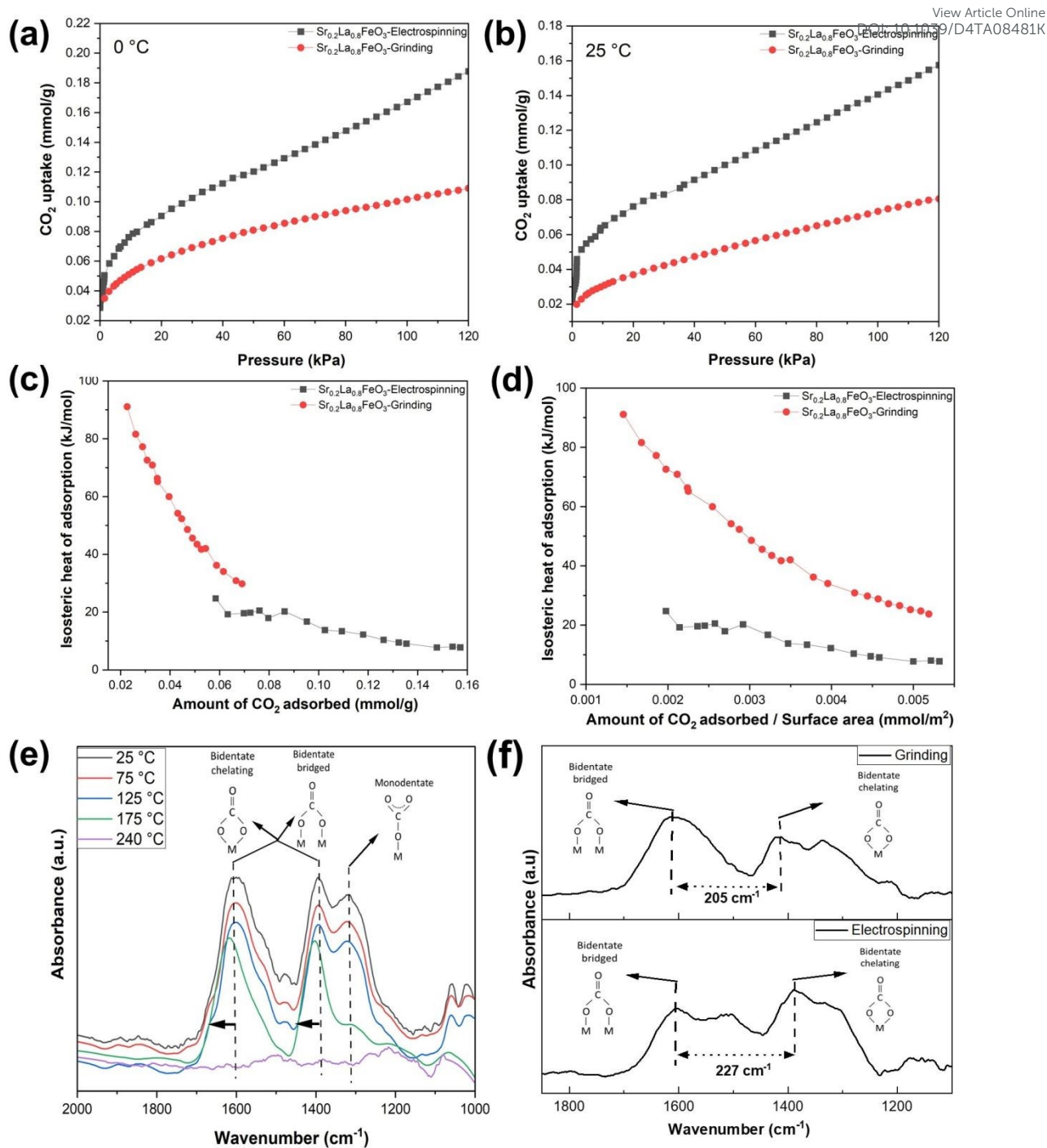


**Figure 5-** (a-b) CO<sub>2</sub> adsorption isotherms of Sr<sub>0.2</sub>La<sub>0.8</sub>FeO<sub>3</sub> at 0 and 25 °C. (c) CO<sub>2</sub> isosteric heats of adsorption. (d) Comparison of isosteric heat of adsorption vs. adsorption capacity per surface area for electrospinning and grinding samples. (e) *In situ* IR spectra of CO<sub>2</sub> adsorbed on Sr<sub>0.2</sub>La<sub>0.8</sub>FeO<sub>3</sub> (Electrospinning) monitored as a function of temperature. (f) *In situ* IR spectra of CO<sub>2</sub> adsorbed in electrospinning and grinding Sr<sub>0.2</sub>La<sub>0.8</sub>FeO<sub>3</sub> at 25 °C.

## Conclusions

CO<sub>2</sub> adsorption using solid sorbents offers a promising approach to carbon capture due to low energy requirements, operational simplicity, and high stability. This study introduces



perovskite oxides as a tunable family of solid sorbents with exceptional structural and compositional flexibility to optimize sorption thermodynamics and kinetics. Using  $\text{Sr}_x\text{La}_{1-x}\text{FeO}_3$  ( $x=0, 0.2, 0.5, \text{ and } 0.7$ ) as a model system, we demonstrated that varying the A-site composition enables a wide range of tunable  $\text{CO}_2$  desorption temperatures ( $75\text{--}500^\circ\text{C}$ ). A strong correlation between surface area and sorption capacity was also established, along with effective methods to enhance the oxide surface area: a salt-assisted grinding method resulted in samples with  $16\text{ m}^2/\text{g}$  whereas an electrospinning method enhanced surface areas to  $\sim 30\text{ m}^2/\text{g}$  from  $3\text{--}5\text{ m}^2/\text{g}$ .

Among the synthesized materials,  $\text{Sr}_{0.2}\text{La}_{0.8}\text{FeO}_3$  prepared via electrospinning exhibited the highest performance, with a moderate desorption temperature (onset:  $120^\circ\text{C}$ , peak:  $240^\circ\text{C}$ ) and a sorption capacity of  $0.68\text{ wt.}\%$ . Adsorption isotherm analysis revealed that  $\text{CO}_2$  chemisorption dominates at low pressures ( $0\text{--}1\text{ kPa}$ ), while physisorption becomes significant at higher pressures. TEM analysis indicated the formation of perovskite nanorods through electrospinning. XPS and (*in-situ*) IR characterizations, coupled with experiment measurements, revealed that near surface La concentrations play a crucial role for reversible  $\text{CO}_2$  sorption. The significant over-representation of La on the surface of the electrospun sample compared to other preparation methods led to a superior surface normalized reversible  $\text{CO}_2$  sorption capacity.

This study highlights the tunability of perovskite oxides as a promising new class of  $\text{CO}_2$  sorbents. While the demonstrated capacity remains lower than that of typical solid sorbents reported to date ( $\sim 1.3\text{--}14\%$ )<sup>47-52</sup>, their high stability and tunability, combined with opportunities for further optimization of surface area and composition, position these oxides as potential candidates for practical applications in  $\text{CO}_2$  capture and utilization.

## Author contributions

Seyedamin Razavi: investigation, and writing – original draft. Vahid Rahmanian: conceptualization- review & editing. Runxia Cai: conceptualization– review & editing. Mahe Rukh: conceptualization. Saad Khan: writing –conceptualization, reviewing and editing, supervision. Fanxing Li: conceptualization, writing – review & editing, supervision, project administration, and funding acquisition.

## Conflicts of interest

There are no conflicts to declare.

## Acknowledgements

This work was supported by the Novo Nordisk Foundation (Grant No. NNF22SA0078767) under the Biocatalyst Interactions with Gases program. We would like to acknowledge Dr. Sonja Salmon's helpful comments and suggestions.

## References

1. B. N. Firtescu, F. Brinza, M. Grosu, E. M. Doaca and A. A. Siriteanu, *Frontiers in Environmental Science*, 2023, **10**.





2. E. S. Sanz-Perez, C. R. Murdock, S. A. Didas and C. W. Jones, *Chem Rev*, 2016, **116**, 11840-11876. View Article Online  
DOI: 10.1039/D4TA08481K
3. D. Welsby, J. Price, S. Pye and P. Ekins, *Nature*, 2021, **597**, 230-234.
4. S. Choi, J. H. Drese and C. W. Jones, *ChemSusChem: Chemistry & Sustainability Energy & Materials*, 2009, **2**, 796-854.
5. M. Yates, J. Blanco, P. Avila and M. Martin, *Microporous and Mesoporous Materials*, 2000, **37**, 201-208.
6. B. B. Saha, S. Koyama, I. I. El-Sharkawy, K. Habib, K. Srinivasan and P. Dutta, *Journal of Chemical & Engineering Data*, 2007, **52**, 2419-2424.
7. H. Yang, Z. Xu, M. Fan, R. Gupta, R. B. Slimane, A. E. Bland and I. Wright, *Journal of environmental sciences*, 2008, **20**, 14-27.
8. T. Ashirov and A. Coskun, *Chimia*, 2024, **78**, 415-422.
9. C. W. Jones, *Annual review of chemical and biomolecular engineering*, 2011, **2**, 31-52.
10. A. Goepfert, M. Czaun, G. S. Prakash and G. A. Olah, *Energy & Environmental Science*, 2012, **5**, 7833-7853.
11. D. M. Ruthven, S. Farooq and K. S. Knaebel, *Pressure swing adsorption*, John Wiley & Sons, 1996.
12. O. Shekhah, Y. Belmabkhout, Z. Chen, V. Guillerm, A. Cairns, K. Adil and M. Eddaoudi, *Nature communications*, 2014, **5**, 4228.
13. F. Brandani and D. M. Ruthven, *Industrial & engineering chemistry research*, 2004, **43**, 8339-8344.
14. R. Wu, E. Carrejo, M. S. Reza, E. Woods, S. Razavi, S. Park, F. Li and W. J. Sagues, *Fuel*, 2024, **373**.
15. L. Brody, M. Rukh, R. Cai, A. Saberi Bosari, R. Schomäcker and F. Li, *Journal of Physics: Energy*, 2023, **5**.
16. R. Cai, K. Yang, X. Wang, M. Rukh, A. S. Bosari, E. Giavedoni, A. Pierce, L. Brody, W. Tang, P. R. Westmoreland and F. Li, *Energy & Environmental Science*, 2024, **17**, 6279-6290.
17. A. Sayari, Y. Belmabkhout and R. Serna-Guerrero, *Chemical Engineering Journal*, 2011, **171**, 760-774.
18. C.-H. Yu, C.-H. Huang and C.-S. Tan, *Aerosol and air quality research*, 2012, **12**, 745-769.
19. M. Li, M. Zhao, F. Li, W. Zhou, V. K. Peterson, X. Xu, Z. Shao, I. Gentle and Z. Zhu, *Nature communications*, 2017, **8**, 13990.
20. Y. Cao, J. Liang, X. Li, L. Yue, Q. Liu, S. Lu, A. M. Asiri, J. Hu, Y. Luo and X. Sun, *Chemical Communications*, 2021, **57**, 2343-2355.
21. B. Koo, K. Kim, J. K. Kim, H. Kwon, J. W. Han and W. Jung, *Joule*, 2018, **2**, 1476-1499.
22. M. Rukh, R. Cai, L. Brody and F. Li, *Chemical Engineering Journal*, 2024, **501**.
23. Y. Zhu, W. Zhou, Z. G. Chen, Y. Chen, C. Su, M. O. Tadé and Z. Shao, *Angewandte Chemie*, 2015, **127**, 3969-3973.
24. C. Borca, B. Xu, T. Komesu, H.-K. Jeong, M. Liu, S.-H. Liou and P. Dowben, *Surface science*, 2002, **512**, L346-L352.
25. W. Lee and B. Yildiz, *ECS Transactions*, 2013, **57**, 2115.
26. E. J. Crumlin, E. Mutoro, Z. Liu, M. E. Grass, M. D. Biegalski, Y.-L. Lee, D. Morgan, H. M. Christen, H. Bluhm and Y. Shao-Horn, *Energy & Environmental Science*, 2012, **5**, 6081-6088.
27. A. Nanning, A. K. Opitz, C. Rameshan, R. Rameshan, R. Blume, M. Hävecker, A. Knop-Gericke, G. n. Rupprechter, B. Klötzer and J. r. Fleig, *The Journal of Physical Chemistry C*, 2016, **120**, 1461-1471.
28. Y. Chen, W. Jung, Z. Cai, J. J. Kim, H. L. Tuller and B. Yildiz, *Energy & Environmental Science*, 2012, **5**, 7979-7988.
29. C. D. Saquing, J. L. Manasco and S. A. Khan, *Small*, 2009, **5**, 944-951.
30. C. A. Bonino, M. D. Krebs, C. D. Saquing, S. I. Jeong, K. L. Shearer, E. Alsberg and S. A. Khan, *Carbohydrate Polymers*, 2011, **85**, 111-119.





31. B. V. Farias, T. Pirzada, R. Mathew, T. L. Sit, C. Opperman and S. A. Khan, *ACS Sustainable Chemistry & Engineering*, 2019, **7**, 19848-19856. View Article Online  
DOI: 10.1039/D4TA08481K
32. J. Xue, T. Wu, Y. Dai and Y. Xia, *Chem Rev*, 2019, **119**, 5298-5415.
33. G. Zheng, J. Jiang, X. Wang, W. Li, J. Liu, G. Fu and L. Lin, *Materials & Design*, 2020, **189**.
34. D. Chen and Y. Zhu, *Nanoscale research letters*, 2017, **12**, 1-5.
35. T. Pirzada, Z. Ashrafi, W. Xie and S. A. Khan, *Advanced Functional Materials*, 2019, **30**.
36. V. Rahmanian, M. Z. Ahmad Ebrahim, S. Razavi, M. Abdelmigeed, E. Barbieri, S. Menegatti, G. N. Parsons, F. Li, T. Pirzada and S. A. Khan, *Journal of Materials Chemistry A*, 2024, **12**, 214-226.
37. Y. Cao, B. Lin, Y. Sun, H. Yang and X. Zhang, *Journal of Alloys and compounds*, 2015, **624**, 31-39.
38. Y. TERAOKA, H.-M. ZHANG and N. YAMAZOE, *Chemistry Letters*, **19**, 5.
39. G. Kulkarni, C. Rao and M. Roberts, *The Journal of Physical Chemistry*, 1995, **99**, 3310-3316.
40. A. Carley, M. Roberts and A. Santra, *The Journal of Physical Chemistry B*, 1997, **101**, 9978-9983.
41. J. Fierro and L. G. Tejuca, *Applied surface science*, 1987, **27**, 453-457.
42. T. H. Fleisch, R. F. Hicks and A. T. Bell, *Journal of Catalysis*, 1984, **87**, 398-413.
43. J. Fierro, *Catalysis today*, 1990, **8**, 153-174.
44. X. Xu, W. Wang, W. Zhou and Z. Shao, *Small Methods*, 2018, **2**, 1800071.
45. S. Richard, A. Mitchell, C. Evans, J. Whitaker, A. Thomson and A. Keith, 2021.
46. G. Busca and V. Lorenzelli, *Materials Chemistry*, 1982, **7**, 89-126.
47. P. Priyadarshini, G. Rim, C. Rosu, M. Song and C. W. Jones, *ACS Environ Au*, 2023, **3**, 295-307.
48. G. Rim, P. Priyadarshini, M. Song, Y. Wang, A. Bai, M. J. Realff, R. P. Lively and C. W. Jones, *J Am Chem Soc*, 2023, **145**, 7190-7204.
49. A. Holewinski, M. A. Sakwa-Novak and C. W. Jones, *J Am Chem Soc*, 2015, **137**, 11749-11759.
50. M. Zhao, J. Xiao, W. Gao and Q. Wang, *Journal of Energy Chemistry*, 2022, **68**, 401-410.
51. J. Wang, H. Huang, M. Wang, L. Yao, W. Qiao, D. Long and L. Ling, *Industrial & Engineering Chemistry Research*, 2015, **54**, 5319-5327.
52. X. Zhu, W. Xie, J. Wu, Y. Miao, C. Xiang, C. Chen, B. Ge, Z. Gan, F. Yang, M. Zhang, D. O'Hare, J. Li, T. Ge and R. Wang, *Chem Soc Rev*, 2022, **51**, 6574-6651.



Data availability statement:

Data supporting this article have been included as part of the Supplementary Information.

Open Access Article. Published on 26 February 2025. Downloaded on 2/26/2025 10:21:15 PM.

This article is licensed under a Creative Commons Attribution-NonCommercial 3.0 Unported Licence.

